Journal of Materials Chemistry A

ROYAL SOCIETY OF CHEMISTRY

PAPER

Cite this: *J. Mater. Chem. A*, 2021, **9**, 423

3D printed carbon aerogel microlattices for customizable supercapacitors with high areal capacitance†

Shijia Yuan,[a] Wei Fan, *[a] Dong Wang,[a] Longsheng Zhang,[b] Yue-E. Miao, [a] Feili Lai [c] and Tianxi Liu *[ab]

Received 5th September 2020
Accepted 30th November 2020

DOI: 10.1039/d0ta08750e

rsc.li/materials-a

Desirable areal and volumetric capacitances of electrodes with high mass loading are of great significance for compact energy storage in practical applications. The key challenge remains in the structural design of electrodes with interconnected micro-/macro-networks for unimpeded electron and ion transport. Herein, three-dimensional (3D) printed carbon aerogel (CA) microlattices are designed with tunable thickness to realize high areal capacitance. By using polyamic acid (PAA) as a crosslinker, graphene oxide/polyamic acid (GP) ink exhibits ideal printability and formability to ensure the continuous printing of self-supported and programmable 3D structures. After subsequent freeze-drying and thermal treatment, the as-obtained CA exhibits not only a well-maintained macrostructure of the extruded shape but also a porous microstructure from the interconnected GP gel. As a result, the 3D printed CA microlattice presents a quasi-proportional increase in areal capacitance with thickness, achieving a desirable areal/volumetric capacitance (870.3 mF cm^{-2}/1.7 F cm^{-3}) under high mass loading (15.3 mg cm^{-2}) and large thickness (4.9 mm). This work offers a promising strategy to construct a customizable structure of a supercapacitor and provides new insights to dramatically improve the energy storage properties of microdevices with limited area.

Introduction

In recent years, wearable electronics have made rapid progress in our daily lives. The intrinsic characteristics of supercapacitors (*e.g.*, high power density and excellent cycling stability) stimulate their exploitation in the field of wearable electronics.[1–4] Achieving high gravimetric capacitance is usually accompanied by the sacrifice of areal and volumetric capacitances.[5,6] Nevertheless, for compact energy storage in practical applications, high energy storage capacity within the limited area or volume is the primary consideration.[7–9] As a result, it is important to construct compact, thick and high-mass-loading electrodes with unimpeded electron and ion transport to obtain desirable areal and volumetric capacitances. Therefore, rigorous requirements are imposed on the structural design of supercapacitors, in which the key is the construction of electrodes with interconnected periodic porous micro/macrostructures.

Significantly, a reasonable structure of the electrode not only provides the device with an improved electrochemical performance, but also meets the pursuit of personalization. However, traditional methods for preparing electrodes usually rely on coating the active materials onto substrates or shaping them *via* molds, which have low preparation efficiency and poor scalability. Unfortunately, these cannot achieve the construction of internal delicate structures.[10–16] Consequently, more efforts are needed to develop new shape-build technologies for the fabrication of advanced electrodes with designable three-dimensional (3D) geometric architectures. It is gratifying that the explosive development of the versatile and efficient 3D printing technology has resulted in new possibilities for designing controllable macrostructures of electrodes.[17–20] Among the different types of 3D printing technologies (such as fused deposition modeling and stereo lithography appearance), direct ink writing (DIW) is able to formulate desirable inks containing versatile components and properties, thus promoting the application of 3D printing in the field of hydrogels and aerogels.[21–39] Recent advances in the field of hydrogels have demonstrated that DIW can be used to construct biological tissues,[21,22] electronic skins,[23,24] smart hydrogels,[25,26] soft actuators,[27] *etc.* Simultaneously, it has been used in the field of aerogels to prepare energy storage devices,[28–30] sensors,[31,32] and

[a]State Key Laboratory for Modification of Chemical Fibers and Polymer Materials, College of Materials Science and Engineering, Innovation Center for Textile Science and Technology, Donghua University, Shanghai 201620, P. R. China. E-mail: weifan@dhu.edu.cn; txliu@fudan.edu.cn; txliu@dhu.edu.cn

[b]Key Laboratory of Synthetic and Biological Colloids, Ministry of Education, School of Chemical and Material Engineering, Jiangnan University, Wuxi 214122, P. R. China

[c]Department of Chemistry, KU Leuven, Celestijnenlaan 200F, 3001 Leuven, Belgium

† Electronic supplementary information (ESI) available. See DOI: 10.1039/d0ta08750e

triboelectric nanogenerators.[33,34] In particular, graphene oxide (GO) has become the most commonly used ink material for 3D printed graphene-based aerogels towards electrochemical applications, which is attributed to the shear thinning rheological behavior and tunable elastic modulus of GO-based inks by adjusting the concentration or adding additives.[35–39] Therefore, it is a feasible strategy to construct diverse graphene-based electrodes with desired micro- and macro-structures *via* DIW-based 3D printing technology.

At present, several researchers have fabricated graphene-based aerogels with precisely programmable macrostructures *via* the DIW-based 3D printing technology, including mesh,[31] interdigitated,[39] and microlattice structures.[35–38] Notably, the premise of the printability is that the GO-based inks need to meet certain rheological characteristics. Specifically, the ink should have a shear thinning behavior to ensure that it can be smoothly extruded from the needle, and a high storage modulus (G') and a correspondingly low loss modulus (G'') under low shear stress to support the printed 3D structure.[28,36] Therefore, in order to meet the standards of printable inks, many strategies have tended to formulate GO gels with high concentrations (>40 mg mL^{-1}) to ensure the high G' required for molding.[35] However, high-concentration GO sheets tend to stack and aggregate, resulting in a high density, blocked pathways for ion diffusion and poor capacitive behavior. Besides, the weak van der Waals attractions between the graphene sheets will lead to the poor mechanical properties of aerogels.[40] In response to these shortcomings, inorganic nanoparticles or organic polymers have been chosen as additives to improve the rheological behavior of GO at lower concentrations and enhance the mechanical properties of aerogels.[28,30] In spite of the high efficiency of this approach, it comes with suboptimal electrical conductivity and the deformation or collapse of the printed structures. Till now, it still remains a great challenge to realize the printability of GO and construct highly conductive and mechanically robust graphene-based aerogels *via* 3D printing technology. Therefore, pursuing a reliable strategy to prepare printable GO inks and resultant aerogels with a designable macrostructure and a porous microstructure is of great significance.

Herein, polyamic acid (PAA) salt has been selected as a crosslinker to prepare the GO/PAA gel, which is used as the printing ink for DIW-based 3D printing technology. Abundant hydrogen bonds between PAA and GO promote the formation of crosslinked networks, which ensures that GO/PAA exhibits relatively high G' for good formability even at a low GO concentration (25 mg mL^{-1}). Carbon aerogels (CAs) after subsequent thermal treatment maintain the crosslinked porous microstructure with N and O-containing moieties introduced simultaneously, improving the mechanical properties of graphene while providing fast electron- and ion-transport to achieve high electrochemical performance. Afterwards, CAs with diverse macrostructures can be prepared by further programming the design to meet the requirements of customizable structures and high areal capacitance of electrodes. Consequently, a flexible fiber-shaped symmetrical supercapacitor based on CAs has been fabricated, which shows excellent areal capacitance (59.1 mF cm^{-2}) and areal energy density (5.3 μW h cm^{-2}). Moreover, CA microlattices have been fabricated and used as self-standing electrodes for supercapacitors. This periodic grid structure maximizes the exposure of active materials and provides sufficient ion-transport channels for electrodes even under high mass loading (15.3 mg cm^{-2}) and large thickness (4.9 mm), ensuring that the areal capacitance of electrodes increases quasi-proportionally with the thickness. Therefore, our strategy achieves the construction of CAs with a designable macrostructure and a highly interconnected porous microstructure, which demonstrates promising applications in the field of energy storage.

Results and discussion

Fabrication and physicochemical characterization of the CA

The preparation process of the 3D printed carbon aerogel (CA) is schematically illustrated in Fig. 1a. In brief, polyamic acid (PAA) salt was added to a stable GO suspension (25 mg mL^{-1}), where the lateral dimensions of the GO sheets are about 0.5–1.5 μm (shown in the TEM image in Fig. S1†). With the addition of triethylamine (TEA), PAA was completely dissolved to form a homogeneous GO/PAA (GP) gel, which ensures smooth and continuous printing by preventing clogging in the nozzle. Subsequently, the gel-state ink was transferred to a syringe and extruded from the needle under air pressure to be shaped according to the designed pattern on a three-axis printing platform (the printing process is shown in Video S1†). After the processes of freeze-drying and thermal treatment, the CA with a specific macrostructure and porous microstructure was obtained. The properties of printed structures are strongly dependent on the rheological properties of inks during the DIW-based 3D printing process. To enable the DIW 3D printing process and good structural formability, we designed GO/PAA gels with suitable rheological behaviors as printing inks for DIW. Due to the strong interaction between the amido group and carbonyl on PAA chains and oxygen-containing functional groups on GO sheets (schematically illustrated in Fig. 1b), PAA can act as a crosslinker to increase the static elastic modulus of GO ink, which effectively guarantees that the extruded filament "sets" immediately, maintains the shape with deposited features and resists the collapse caused by gravity and surface tension. Remarkably, during extrusion, the hydrogen bond is disconnected and the crosslinking network is relaxed to allow the ink to flow continuously. And after squeezing out of the needle, the reversible hydrogen bonds will quickly recover to restore the platform modulus, thereby ensuring the ideal formability of the ink. To further verify the effect of the PAA content on the moldability of the ink, GP-x inks with different ratios of GO to PAA (where x represents the mass ratio of GO to PAA) were prepared (Fig. S2a†), and the corresponding digital photos are shown in Fig. 1c. It can be seen that the shape of pure GO and GP-6 will collapse due to the low static elastic modulus, while GP-4 and GP-2 can still maintain the stereoscopic shape and remain stable even when the substrate is inclined at an angle of 40 degrees, indicating that the moldability of the ink is gradually enhanced with the addition of PAA.

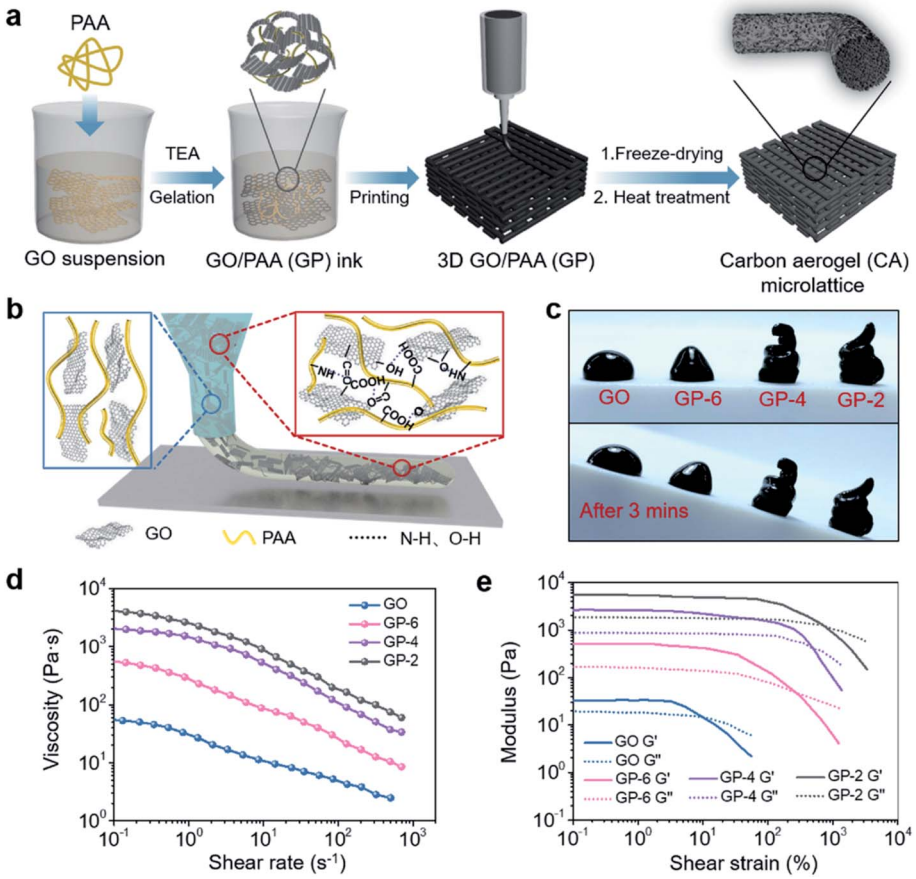

Fig. 1 Fabrication process of the CA and rheological behaviors of GP inks. (a) Schematic illustration for the fabrication process of the CA microlattice. (b) Mechanism of reversible hydrogen bonding between GO and PAA. (c) Optical images showing the ability of GO and GP-*x* inks to maintain the extruded shape on a flat or inclined polytetrafluoroethylene substrate. (d) Log–log plots of apparent viscosity *versus* shear rate of GO and GP-*x* inks. (e) Log–log plots of the storage modulus (G') and loss modulus (G'') as a function of shear strain.

Simultaneously, Fig. S2b† shows that the GP-4 can adhere to the bottom in an inverted bottle, indicating that the ink is in a gel state when the ratio of GO to PAA is 4 : 1. A specific explanation can be obtained from the analysis of rheological data. From the log–log plots of apparent viscosity *versus* shear rate in Fig. 1d, it can be observed that the initial viscosity of the samples gradually increases with the increase of the content of PAA, which is due to the enhanced crosslinking network between PAA chains and GO sheets. And all samples show shear thinning behavior, which is conducive to the continuous extrusion of ink from the needle. Fig. 1e exhibits the storage modulus (G') and loss modulus (G'') of different samples as a function of shear strain. When the content of PAA increases, the platform for the G' of the ink increases from 50 Pa (pure GO) to 2500 Pa (GP-4) and 5500 Pa (GP-2), respectively. This is due to the denser crosslinking network that enables the ink to convert more external energy into elastic energy. As a result, the rheological properties of the ink can be adjusted by regulating the content of PAA to achieve satisfactory printing ability. After taking the above rheological properties and conductivity of ink into consideration, GP-4 ink with a ratio of GO to PAA of 4 : 1 is selected and used in the following work.

The digital photographs in Fig. 2a present the printed GP-4 hydrogel microlattice, indicating the ink can maintain the printed 3D architecture. Then the printed structure can be retained after freeze-drying, and lightweight CA-4 can be obtained after subsequent imidization and carbonization. As shown in Fig. 2b, an aerogel microlattice with a size of 1.5 cm × 1.5 cm × 0.5 cm can stand on bristlegrass, indicating its lightweight nature. Other complex structures, such as the grid barrel structure presented in Fig. 2c, can be further prepared by proper structural design. Besides, the printed CA-4 has anti-compressive ability, as demonstrated by compressive and tensile tests on the CA-4 microlattice in Fig. S3.† The out-of-plane compressive strength and modulus are 25.4 kPa and 306.9 kPa, while that of in-plane compression are 13.1 kPa and 131.4 kPa, respectively. Additionally, the tensile strength and modulus are 10.5 kPa and 213.8 kPa. Compared with other elastic graphene aerogels,[31,41,42] the CA-4 has the characteristics of stiffness and anti-compressive ability, which ensures its good structural stability as an electrode. As illustrated in Fig. 2d, the aerogel with a chair-like structure can withstand over 200 times its own weight. Fig. 2e–g show the SEM images of a printed single fibrous CA-4. From Fig. 2e and f, the cross-sectional

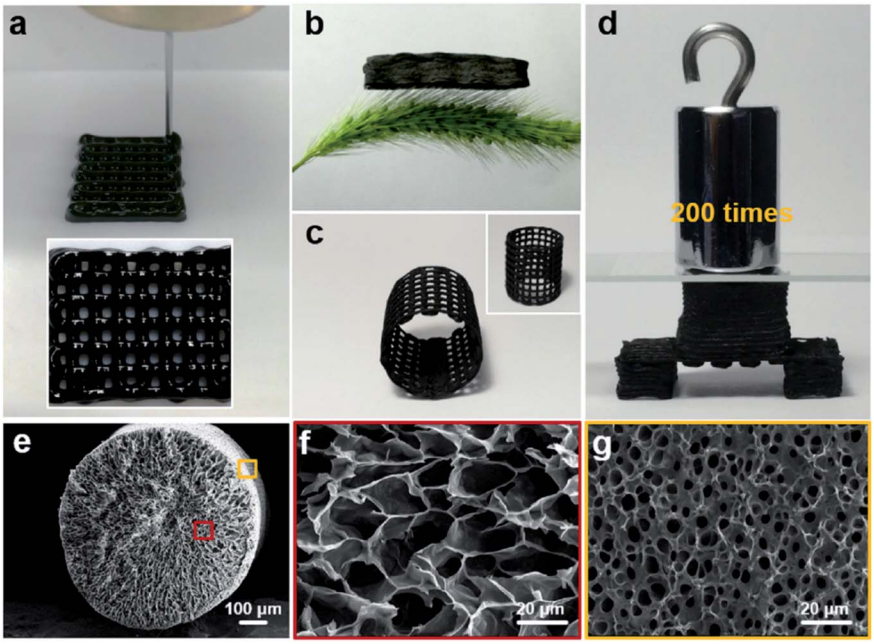

Fig. 2 Structural and morphological characterization of CA-4. (a) GP-4 hydrogel microlattice before freeze-drying. (b) CA-4 with a cubic lattice structure stands on bristlegrass. (c) CA-4 with a grid barrel structure. (d) CA-4 with a chair-like structure can withstand over 200 times its own weight. (e) Cross-sectional SEM image of the single fibrous CA-4 at low magnification. (f) Cross-sectional morphology and (g) surface morphology of fibrous CA-4 at high magnifications, corresponding to the red and yellow squares in Fig. 2e, respectively.

morphology of the CA-4 exhibits a uniform macroporous network. The macropores can serve as ion storage buffers, and the interconnected network contributes to accelerated ion transport, thus providing fast electrochemical response. Besides, the surface of the CA-4 also exhibits uniform macropores (Fig. 2g and S4†), which are derived from the sublimation of ice crystals on the surface during the freeze-drying process. This is beneficial for the penetration of the electrolyte inside the electrodes. Additionally, Fig. S5† further compares the cross-sectional morphology of fibrous CAs prepared with different proportions of GO and PAA. The CA formed with pure GO and CA-6 shows loose lamellar stacking and the graphene sheets tend to accumulate, which results mechanical brittleness and they cannot be assembled into a device (Fig. S5a–d†), while CA-2 exhibits a similar morphology to CA-4 (Fig. S5e and f†), indicating that a crosslinking porous network can be formed only when the content of PAA reaches more than 1/4. Hence, the content of PAA plays an important role in the construction of the microstructure, thus affecting the electrochemical performance of the resultant CA.

Existing studies have shown that CAs carbonized with organic gels usually contain certain heteroatoms, which will introduce additional pseudo-capacitance and enhance wettability. Therefore, in order to confirm that PAA will introduce surface functionalization after heat treatment, we have analyzed the composition of the CA. Energy dispersive spectrum (EDS) mapping (Fig. S6a†) shows that the C element was uniformly distributed on the carbon skeleton with 3D macropores, with a small amount of N and O elements evenly distributed. The N-doping feature benefited from amino groups on PAA chains. The elemental species was further analyzed based on X-ray photoelectron spectroscopy (XPS). As illustrated in Fig. S6b,† the CA and CA-4 present signals of the C1s peak and O1s peak at about 284.8 eV and 533.0 eV, respectively. Notability, the O content in CA-4 (5.1%) is higher than that in the CA (3.4%) (Table S1†). Additionally, CA-4 has an extra N1s peak at 400.0 eV, which indicates that N atoms were successfully doped into the carbon lattice. The high-resolution N1s spectrum (Fig. S6c†) can be deconvoluted to pyridinic N (N-6, 398.4 eV), pyrrolic N (N-5, 400.4 eV), graphitic N (N-Q, 401 eV) and pyridine-N-oxide (N-X, 402.6 eV).[6,43] It is reported that N-doped CAs with a porous network structure provide an efficient pathway for ion diffusion and facilitate electron transport, which is considered to contribute to enhancing the specific capacitance.[43] The deconvolution of the C1s spectrum of CA-4 suggests five components, including C=C (284.6 eV), C–N (285.2 eV), C–O (286.3 eV), C=O (287.8 eV), and O–C=O (289.2 eV) (Fig. S6d†). Some previous references demonstrate that the O-containing moieties can improve the wettability of porous carbon materials and facilitate the penetration of the electrolyte,[52,53,56] which is also confirmed by the contact angle test (Fig. S6e and f†). However, the introduction of heteroatoms will induce a certain degree of disorder of carbon materials which can be authenticated using the Raman spectra (Fig. S6g†). Therefore, N and O-containing moieties were introduced in CA-4, which would enhance the electrochemical performance by facilitating electron transport and electrolyte penetration.

Electrochemical investigations of CA-*x* fiber-shaped symmetric supercapacitors (FSSCs)

Since the large planar structure limits the development of wearable energy storage devices, it is necessary to construct

fibrous wearable devices.[43–49] The preparation of fibrous CAs by 3D printing avoids complicated procedures such as wet spinning, exhibiting high efficiency and scalability. We used these 3D printed fibrous CAs as electrodes and assembled them into all-solid-state FSSCs (schematically presented in Fig. S7†), and the corresponding electrochemical performance is exhibited in Fig. 3. The schematic in Fig. 3a illustrates the important role played by the constructed morphology of the CA in device operation. The macropores on the fiber surface promote the electrolyte penetration inside the electrode, while the internal macropores serve as a charge storage buffer to improve the capacitance behavior. The electrochemical performances of the FSSCs assembled from the fibrous CA-6, CA-4, and CA-2 were compared first. The cyclic voltammogram (CV) profiles of all the FSSCs present nearly rectangular shapes, illustrating the characteristic of the major double layer capacitors. Besides, the O- and N-functionalities can modify the local electronic structure of the CA and contribute a small amount of extra pseudocapacitance.[43] And it can be found that the CV curve of the CA-4 FSSC exhibits the largest enclosed area, directly indicating that it has the highest specific capacitance (Fig. S8a†). The longer discharge time of the CA-4 FSSC in the galvanostatic charge–discharge (GCD) curve can also confirm this result (Fig. S8b†). The cause of the capacitance difference can be further analyzed from the electrochemical impedance spectroscopy (EIS) results in Fig. 3b. The fitted equivalent circuit of the CA-*x* FSSC is represented in Fig. S9,† and the fitting parameters are listed in Table S2.† It can be clearly observed from the inset that the CA-4 FSSC has a smaller *x*-intercept than the CA-2 FSSC, indicating that the CA-4 FSSC has a smaller equivalent series resistance (R_s) (32.8 Ω < 64.1 Ω), which benefits from the higher conductivity of the CA-4 electrode (22.3 S cm^{-1} > 7.8 S cm^{-1}, shown in Fig. S10†). PAA can be effectively carbonized after high temperature to form an unobstructed conductive channel. However, with the introduction of heteroatoms, the degree of graphitization will be reduced as the PAA content increases (as indicated in the Raman spectra in Fig. S6g†), leading to reduced conductivity and larger internal resistance as for CA-2. In the low-frequency region, the CA-4 FSSC has a more vertical line than the CA-6 FSSC, illustrating that it has a faster electrolyte ion diffusion rate. This is attributed to the interconnected porous network in the CA-4 electrode due to the appropriate amount of PAA as the crosslinking agent, which provides a fast channel for ion transport. Therefore, combined with good electrical conductivity and more favorable microstructure, the CA-4 FSSC demonstrates outstanding specific capacitance and better electrochemical performance.

Then we performed a comprehensive evaluation of the electrochemical performance of the CA-4 FSSC. The optimum voltage window is 0.8 V and the CV curve still maintains a nearly rectangular shape at a high scan rate of 200 mV s^{-1}, revealing its good rate performance (Fig. S11a and b†). The GCD curve in Fig. S11c† displays a symmetrical triangular profile, verifying the electric double layer capacitance characteristics. And the

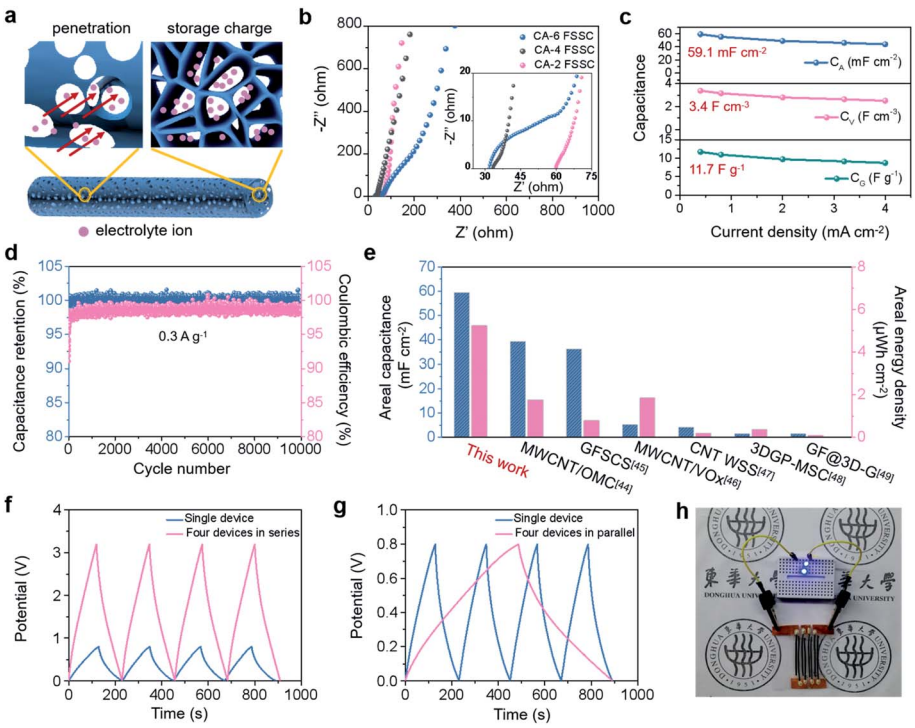

Fig. 3 Electrochemical performance of the CA-*x* fiber-shaped symmetric supercapacitor (FSSC). (a) Schematic of the operation of the CA-based FSSC. (b) Nyquist plots of the CA-*x* FSSC (*x* = 2, 4, 6). (c) Specific capacitance and the corresponding capacitance retention of the CA-4 FSSC at different current densities. (d) Cycling stability and coulombic efficiency of the CA-4 FSSC at a current density of 0.3 A g^{-1}. (e) Comparison of the areal capacitance and areal energy density in this work with those in other works. (f) GCD curves of four CA-4 FSSCs in series. (g) GCD curves of four CA-4 FSSCs in parallel. (h) Optical image of four CA-4 FSSCs in series lighting two blue LEDs.

capacitance values of the CA-4 FSSC under different current densities are calculated in Fig. 3c. For linear supercapacitors, the mass of the electrodes is usually low, while limited space is the key factor. Therefore, the specific capacitance based on the area or volume is more valuable for evaluation. It can be seen that the areal capacitance of the CA-4 FSSC at 0.4 mA cm^{-2} is 59.1 mF cm^{-2} (the corresponding volumetric capacitance is 3.4 mF cm^{-3}, and the gravimetric capacitance is 11.7 F g^{-1}). In addition, as the current density increases, the capacitance shows a slow downward trend, indicating the good rate performance of the CA-4 FSSC. Fig. 3d displays the capacitance retention and coulombic efficiency of the CA-4 FSSC after 10 000 cycles of charging and discharging at 0.3 A g^{-1}. The capacitance has almost no attenuation and the Coulomb efficiency is as high as 99%, demonstrating the desirable cycling stability. The CA-4 FSSC exhibits outstanding areal capacitance and areal energy density, which reaches 5.3 μW h cm^{-2} at a power density of 0.2 mW cm^{-2} and surpasses those of most previously reported carbon-based devices as summarized in Fig. 3e and S11d.†[44–49] These excellent electrochemical properties of the CA-4 FSSC are the result of the combined effect of high electrical conductivity and the N-doped interconnected porous structure. To meet the high voltage and large capacitance required in practical applications, we connected several individual CA-4 FSSCs in series and parallel to assemble integrated devices (Fig. S12†). As seen in Fig. 3f and S12b,† when four CA-4 FSSCs are connected in series, the voltage window is increased by 4 times to 3.2 V, while the area of the CV curve and the discharge time are almost unchanged, indicating that the capacitance remains at the original value. When four CA-4 FSSCs are connected in parallel, the voltage window is still 0.8 V, but the capacitance value is increased by 4 times (Fig. 3g and S12c†). As a demonstration, four CA-4 FSSCs in series can illuminate two parallel LED bulbs with a voltage of 1.8 V (Fig. 3h), indicating that the integrated device assembled with the CA-4 FSSCs has great potential for practical applications.

Electrochemical investigations of the 3D printed CA-4 microlattice

In conventional thick-bulk electrodes, the thick electrode is detrimental to electrolyte penetration with the increase of loading mass, resulting in the dead zone of active materials.[50–56] In contrast, 3D printed microlattice structures provide sufficient ion and electron transport pathways from the bottom to the top of the electrode.[35–38] As a result, the active material can fully exert its electrochemical performance, so that the areal capacitance increases quasi-proportionally with the increase of the loading mass. Here, we constructed a microlattice structure of CA-4 with different layer numbers, including 2, 4, 6, and 8 layers with corresponding thicknesses of 1.4 mm, 2.8 mm, 4.1 mm, and 4.9 mm, respectively, which were used as self-supporting electrodes (as shown in Fig. 4a). Specifically, the increasing trend in the mass and thickness of the electrode with the number of layers is illustrated in Fig. 4a. It is obvious that the mass increases linearly with the increase of layers, with a mass loading of 15.3 mg cm^{-2} for 8 layers, but the thickness slightly deviates from the linear value when it reaches 8 layers. The linear deviation of thickness with the number of printed layers is due to the squashed ink at the bottom by the gravity of the multilayer above it. This is why we choose the layer number instead of thickness as the variable to explain the growth trend of the capacitance, which is in line with the controllability required in the actual manufacturing process. The corresponding electrochemical performance of the CA-4 microlattice was studied in a three-electrode system with H_2SO_4 as the electrolyte. The resistance values of the CA-4 microlattice with different layer numbers have little difference as shown by the EIS curves in Fig. 4b, illustrating that the ion- and electron-

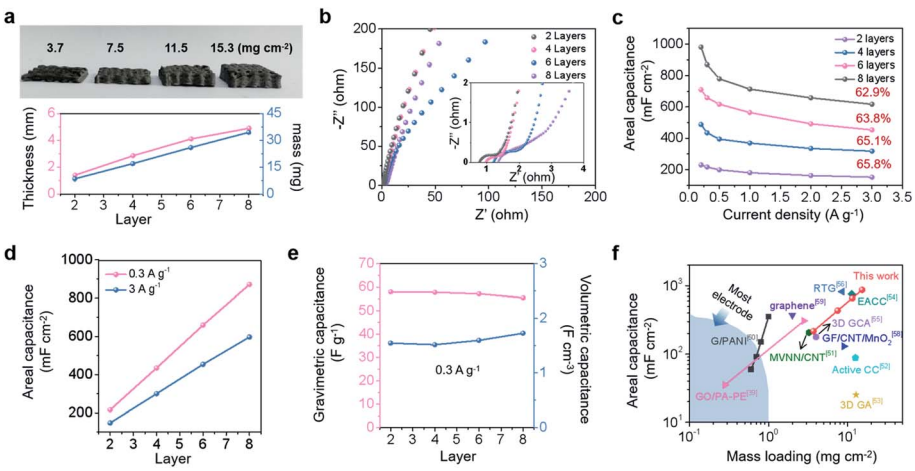

Fig. 4 Electrochemical performance of the 3D printed CA-4 microlattice. (a) Optical image of CA-4 microlattice electrodes with different layer numbers, and plots of thickness and mass of electrode as a function of layer number. (b) Nyquist plots of the CA-4 microlattice electrodes with different layer numbers. (c) Areal capacitance of the CA-4 microlattice electrodes with different layer numbers at different current densities. (d) Areal capacitance of the electrodes measured at 0.3 and 3 A g^{-1} plotted as a function of layer number. (e) Gravimetric and volumetric capacitances of the CA-4 microlattice electrode with different layer numbers. (f) Comparison of the areal capacitances of the CA-4 microlattice electrode with those of previously reported electrodes.

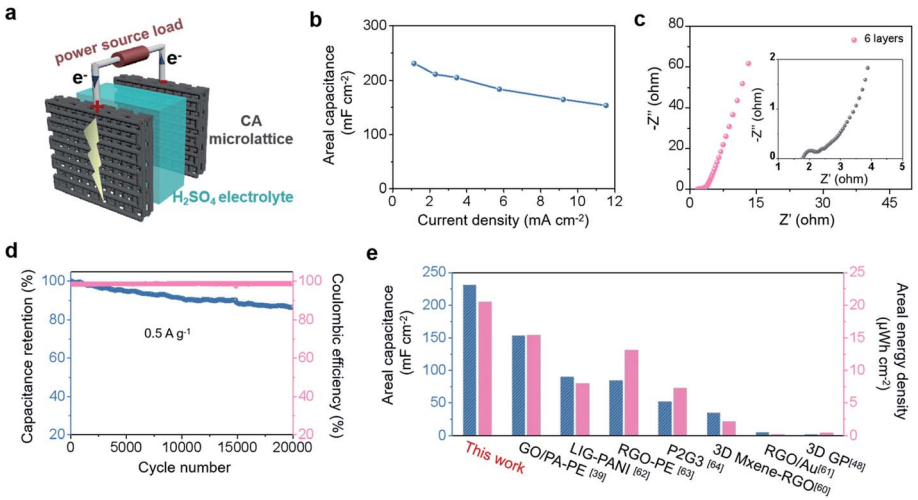

Fig. 5 Electrochemical performance of a symmetric supercapacitor assembled using the CA-4 microlattice with 6 layers. (a) Schematic illustration of a symmetric supercapacitor tested in an aqueous electrolyte. (b) Areal capacitance tested at different current densities. (c) Nyquist plots. (d) Capacitance retention and coulombic efficiency tested at a current density of 0.5 A g^{-1} for 20 000 cycles. (e) Comparison of the areal specific capacitance and areal energy density in this work with those in other work.

transport are not significantly affected by the increase of the electrode thickness. This result is attributed to the interconnected porous microstructure containing surface functionalization and a latticed macrostructure, which jointly provide unobstructed channels for electrons and ions. The CV curves of the CA-4 microlattice electrode with 6 layers still maintain a regular rectangle at a high scan rate of 1000 mV s^{-1} (Fig. S13a and b†), which also reveals the high-speed transport of electrolyte ions even in thick electrodes. Based on the GCD curves (Fig. S13c†), the areal capacitance at different current densities can be calculated (Fig. 4c). The areal capacitance of the CA-4 microlattice with 6 layers is 658.9 mF cm^{-2} at a current density of 0.3 A g^{-1} (3.5 mA cm^{-2}), while that for the 8-layer electrode can reach 870.3 mF cm^{-2} at a current density of 0.3 A g^{-1} (4.6 mA cm^{-2}). In thicker electrodes, the electrolyte is still able to penetrate sufficiently due to the porous microstructure and latticed macrostructure of the CA-4 microlattice, so that a fast kinetic response can be ensured even at large current densities to achieve high rate performance. Therefore, whether at a low current density of 0.3 A g^{-1} or high current density of 3 A g^{-1}, the areal capacitance shows a tendency to increase in proportion to the number of layers (Fig. 4d). Remarkably, the gravimetric and volumetric capacitances of CA-4 microlattice electrodes with different layer numbers all have similar values, illustrating that there is no attenuation at high mass loading (Fig. 4e). The 8-layer CA-4 microlattice achieves a satisfactory gravimetric capacitance of 55.5 F g^{-1} at a current density of 0.3 A g^{-1} and volumetric capacitance of 1.7 F cm^{-3} at a current density of 9.4 mA cm^{-3}, demonstrating that the microlattice structure is conducive to the active material to fully contribute its own capacitance even in the thickest electrode with 4.9 mm. The CA-4 microlattice electrode achieves an impressive areal capacitance under high mass loading, which is higher than those of the previously reported carbon and functionalized carbon electrodes (Fig. 4f and Table S3†).[39,50–59]

In order to understand the actual performance of a complete device, we further tested the assembled symmetrical supercapacitors by using the 6-layer CA-4 microlattice as the electrode in a two-electrode system (Fig. 5a). Fig. S14a and b† show that the CV curves of a symmetric cell are rectangular in shape in the optimal voltage window of 0.8 V, and the GCD curves in Fig. S14c† show a symmetrical triangular profile, which jointly illustrate the characteristics of the electrical double layer. Fig. 5b displays the areal capacitances of a symmetric cell at different current densities. When the current density is 1.2 mA cm^{-2}, the areal capacitance is 230.7 mF cm^{-2}, and it still remains at 153.8 mF cm^{-2} even at 11.5 mA cm^{-2}, indicating good rate performance. The small x-intercept in the high frequency region and the nearly vertical line in the low frequency region in Fig. 5c illustrate that fast electron- and ion-transport occur in the symmetric device. Fig. 5d shows that the symmetrical device has a capacitance retention of 81% and a coulombic efficiency of 99% after 20 000 cycles, demonstrating that the device has desirable electrochemical stability. We further calculated the areal energy density and areal power density of the symmetrical device (presented in the Ragone plot in Fig. S14d†). The areal energy density can be as high as 20.5 μW h cm^{-2} at a power density of 0.9 mW cm^{-2} and still remains at 13.7 μW h cm^{-2} at a power density of 11.5 mW cm^{-2}. The areal capacitance and areal energy density of the CA-4 microlattice based symmetrical device surpass those of most previously reported carbon-based devices, indicating the dominant performance of the symmetrical device prepared in this work (Fig. 5e).[39,48,60–64]

Conclusion

In summary, we adopted advanced 3D printing technology to prepare designable carbon aerogels (CAs) and assembled them into an integrated supercapacitor to satisfy the needs of

wearable electronic devices for high electrochemical performance and personalization. By adding a certain amount of PAA as the crosslinker, the reversible hydrogen bond between GO and PAA can effectively regulate the rheological properties to ensure that the GO/PAA (GP) ink is suitable for molding by direct ink writing. The derived CA has both a controllable macrostructure and a highly interconnected porous microstructure, as well as N and O-containing moieties, which together facilitate the fast transport for electrons and ions and penetration of electrolytes. Then fibrous CA-4 with excellent electrical conductivity was assembled into an all-solid-state fiber-shaped symmetrical device (FSSC), which exhibits prominent areal capacitance (59.1 mF cm^{-2}) and areal energy density (5.3 μW h cm^{-2}). Furthermore, the CA-4 microlattice electrode with high mass loading was constructed, and its areal capacitance increases quasi-proportionally with the thickness, indicating efficient ion diffusion and a fast kinetic response even in thick electrodes. The CA-4 microlattice electrode exhibits an areal capacitance of up to 870.3 mF cm^{-2} at a high mass loading of 15.3 mg cm^{-2} and large thickness of 4.9 mm, without sacrificing its gravimetric and volumetric capacitive performance. The results suggest their great potential for practical application and open up high possibilities for area-limited microdevices with outstanding electrochemical performance.

Experimental section

Preparation of the GO/PAA (GP) ink

0.5 g of graphene oxide (GO) powder (prepared by a modified Hummers method) was dispersed in deionized water and a stable suspension (20 mL, 25 mg mL^{-1}) was obtained after 2 h of sonication. Then 0.125 g of triethylamine (TEA) capped polyamic acid salt (PAA) precursors (prepared based on our previous work[65]) and 0.06 g TEA were added to the GO suspension, and a homogeneous GO/PAA sol was obtained after thorough stirring. Afterwards, the sol was left to undergo sol–gel transformation to obtain a viscoelastic GO/PAA hydrogel, and it was abbreviated as GP-4, where 4 represents the mass ratio of GO to PAA. Meanwhile, by adjusting the mass ratio of GO to PAA, GO (without PAA), GP-6 and GP-2 can be fabricated, respectively.

Ink rheology

The rheological properties were tested using a stress-controlled rheometer (Mars 60) equipped with a 20 mm-flat plate, and the gap is 1 mm. Specifically, the viscosity of the ink was analyzed at a shear rate scan range of 0.01 to 1000 s^{-1} to characterize the shear thinning behavior. And the storage modulus (G') and loss modulus (G'') of the ink were measured by oscillation strain sweep (0.01–1000%) at a frequency of 1 Hz.

3D printing process and fabrication of the carbon aerogel (CA)

The prepared ink was filled into a 30 mL syringe barrel equipped with a cylindrical nozzle having a diameter from 400 μm to 800 μm. Then the syringe barrel was placed in a defoamer and centrifuged at 1500 rpm for 10 min to remove air bubbles to obtain a homogeneous ink. Afterwards, the ink-filled syringe was mounted on a three-axis dispenser (RZC-30WK, China). For printing, the ink was squeezed out of the needle under an air pressure of about 250 kPa. After printing was completed at a speed of 4 mm s^{-1}, the GO/PAA gel with a specific macrostructure was placed in a liquid nitrogen atmosphere for freezing. Then the GO/PAA aerogel could be obtained after subsequent freeze-drying for 48 h in a freeze dryer (FreezeZone, Labconco Corporation, USA). Finally, the obtained precursor aerogel was thermally imidized at 300 °C for 2 h under a nitrogen atmosphere to convert PAA to polyimide and further carbonized at 800 °C for 2 h to obtain a carbon aerogel (CA) with a specific structure. The CA derived from GO/PAA ink with different PAA ratios was named CA-x, where x represents the mass ratio of GO to PAA.

Characterization

The morphology of the aerogels was investigated using a field emission scanning electron microscope (FESEM, Ultra55) with an EDS detector. The size of GO sheets was characterized by transmission electron microscopy (TEM, JEM-2100, JEOL). The structure and composition of the samples were measured by Raman spectroscopy (inVia-Reflex, Renishaw, 532 nm). A digital multimeter (Keithley 2612B) was used to measure electric resistance at a sampling interval of 2 Hz using the two-probe method. X-ray photoelectron spectroscopy (XPS) was performed using a spectrometer (Escalab 250Xi) with Al Kα X-ray radiation.

Electrochemical measurements

Electrochemical testing was performed on an electrochemical working station (CHI660E, Shanghai, China). Using a three-electrode system, the printed CA microlattices (15 cm × 10 cm × h, h represents the thickness of CAs with different layer numbers (2 layers: 1.4 mm; 4 layers: 2.8 mm; 6 layers: 4.1 mm; 8 layers: 4.9 mm)) served as self-standing electrodes, Ag/AgCl was used as the reference electrode, and the test was completed in a 1 M H_2SO_4 electrolyte. The specific capacitance of a single electrode was determined using the following equations:

$$C_G = \frac{It}{mV} \quad (1)$$

$$C_A = \frac{It}{sV} \quad (2)$$

$$C_V = \frac{It}{vV} \quad (3)$$

in which C_G, C_A and C_V are the gravimetric, areal, and volumetric capacitance (F g^{-1}, mF cm^{-2}, and F cm^{-3}), I represents the discharge current (A), t represents the discharge time (s), and V represents the voltage window. m represents the total mass (g) of the electrode, s is the surface area (cm^2) and v is the volume (cm^3) of the geometric electrode.

A two-electrode system was used to measure the electrochemical performance of the integrated CA-x fiber-shaped symmetrical supercapacitor (FSSC) and symmetrical devices

were assembled with the CA electrode with 6 layers in the 1 M H_2SO_4 electrolyte. The areal energy density (E, μW h cm^{-2}) and areal power density (P, mW cm^{-2}) of a symmetric supercapacitor can be calculated from the following equations:

$$E_A = \frac{1}{2} C_A V^2 \quad (4)$$

$$P_A = \frac{E_A}{t} \quad (5)$$

where C_A represents the areal capacitance (mF cm^{-2}) of the symmetric supercapacitor, V represents the operating voltage (V), and t represents the discharge time (s).

Conflicts of interest

The authors declare no conflict of interest.

Acknowledgements

The authors are grateful for the financial support from the National Natural Science Foundation of China (21704014, 21674019, and 52073053), the Fundamental Research Funds for the Central Universities (2232019A3-03), the Shanghai Municipal Education Commission (17CG33), the Shanghai Scientific and Technological Innovation Project (18JC1410600), and the Shanghai Sailing Program (17YF1400200).

References

1 T. Lv, M. Liu, D. Zhu, L. Gan and T. Chen, *Adv. Mater.*, 2018, **30**, 1705489.
2 T. Q. Trung and N. Lee, *Adv. Mater.*, 2017, **29**, 1603167.
3 T. An and W. Cheng, *J. Mater. Chem. A*, 2018, **6**, 15478–15494.
4 J. Zhao, J. W. Gong, G. L. Wang, K. Zhu, K. Ye, J. Yan and D. X. Cao, *Chem. Eng. J.*, 2020, **401**, 125456–125462.
5 Z. Pan, H. Zhi, Y. Qiu, J. Yang, L. Xing, Q. Zhang, X. Ding, X. Wang, G. Xu, H. Yuan, M. Chen, W. Li, Y. Yao, N. Motta, M. Liu and Y. Zhang, *Nano Energy*, 2018, **46**, 266–276.
6 D. Wang, W. Fan, S. Yuan and T. X. Liu, *Electrochim. Acta*, 2019, **323**, 134811–134820.
7 J. Li, N. Wang, J. Tian, W. Qian and W. Chu, *Adv. Funct. Mater.*, 2018, **28**, 1806153.
8 G. Qu, J. Cheng, X. Li, D. Yuan, P. Chen, X. Chen, B. Wang and H. Peng, *Adv. Mater.*, 2016, **28**, 3646.
9 S. Padmajan Sasikala, K. E. Lee, J. Lim, H. J. Lee, S. H. Koo, I. H. Kim, H. J. Jung and S. O. Kim, *ACS Nano*, 2017, **11**, 9424–9434.
10 F. L. Lai, C. Yang, R. Q. Lian, K. B. Chu, J. J. Qin, W. Zong, D. W. Rao, J. Hofkens, X. H. Lu and T. X. Liu, *Adv. Mater.*, 2020, **32**, 2002474.
11 X. Wang, Y. Zhang, C. Zhi, X. Wang, D. Tang, Y. Xu, Q. Weng, X. Jiang, M. Mitome, D. Golberg and Y. Bando, *Nat. Commun.*, 2013, **4**, 2905.
12 L. Li, Y. Zhang, H. Y. Lu, Y. F. Wang, J. S. Xu, J. X. Zhu, C. Zhang and T. X. Liu, *Nat. Commun.*, 2020, **11**, 62.
13 G. Wang, X. Sun, F. Lu, H. Sun, M. Yu, W. Jiang, C. Liu and J. Lian, *Small*, 2012, **8**, 452.
14 Y. J. Wang, Y. Cui, Z. Y. Shao, W. W. Gao, W. Fan, T. X. Liu and H. Bai, *Chem. Eng. J.*, 2020, **390**, 124623–124630.
15 J. Chen, J. Xu, S. Zhou, N. Zhao and C. Wong, *Nano Energy*, 2016, **25**, 193–202.
16 Z. Huang, H. Guo and C. Zhang, *Compos. Commun.*, 2019, **12**, 117–122.
17 Y. Wang, C. Chen, H. Xie, T. Gao, Y. Yao, G. Pastel, X. Han, Y. Li, J. Zhao, K. K. Fu and L. Hu, *Adv. Funct. Mater.*, 2017, **27**, 1703140.
18 H. Wei, X. Cauchy, I. O. Navas, Y. Abderrafai, K. Chizari, U. Sundararaj, Y. Liu, J. Leng and D. Therriault, *ACS Appl. Mater. Interfaces*, 2019, **11**, 24523–24532.
19 F. Zhang, M. Wei, V. V. Viswanathan, B. Swart, Y. Shao, G. Wu and C. Zhou, *Nano Energy*, 2017, **40**, 418–431.
20 M. Wei, F. Zhang, W. Wang, P. Alexandridis, C. Zhou and G. Wu, *J. Power Sources*, 2017, **354**, 134–147.
21 Z. Wang, G. An, Y. Zhu, X. Liu, Y. Chen, H. Wu, Y. Wang, X. Shi and C. Mao, *Mater. Horiz.*, 2019, **6**, 733–742.
22 L. Shao, Q. Gao, C. Xie, J. Fu, M. Xiang and Y. He, *Adv. Healthcare Mater.*, 2019, **8**, 1901142.
23 S. Wei, G. Qu, G. Luo, Y. Huang, H. Zhang, X. Zhou, L. Wang, Z. Liu and T. Kong, *ACS Appl. Mater. Interfaces*, 2018, **10**, 11204–11212.
24 Y. Zhou, M. Layani, S. Wang, P. Hu, Y. Ke, S. Magdassi and Y. Long, *Adv. Funct. Mater.*, 2018, **28**, 1705365.
25 Z. Chen, D. Zhao, B. Liu, G. Nian, X. Li, J. Yin, S. Qu and W. Yang, *Adv. Funct. Mater.*, 2019, **29**, 1900971.
26 H. Arslan, A. Nojoomi, J. Jeon and K. Yum, *Adv. Sci.*, 2019, **6**, 1800703.
27 S. Y. Zheng, Y. Shen, F. Zhu, J. Yin, J. Qian, J. Fu, Z. L. Wu and Q. Zheng, *Adv. Funct. Mater.*, 2018, **28**, 1803366.
28 X. Tang, C. Zhu, D. Cheng, H. Zhou, X. Liu, P. Xie, Q. Zhao, D. Zhang and T. Fan, *Adv. Funct. Mater.*, 2018, **28**, 1805057.
29 P. He, X. Tang, L. Chen, P. Xie, L. He, H. Zhou, D. Zhang and T. Fan, *Adv. Funct. Mater.*, 2018, **28**, 1801121.
30 Y. Jiang, Z. Xu, T. Huang, Y. Liu, F. Guo, J. Xi, W. Gao and C. Gao, *Adv. Funct. Mater.*, 2018, **28**, 1707024.
31 F. Guo, Y. Jiang, Z. Xu, Y. Xiao, B. Fang, Y. Liu, W. Gao, P. Zhao, H. Wang and C. Gao, *Nat. Commun.*, 2018, **9**, 881.
32 Q. Zhang, F. Zhang, S. P. Medarametla, H. Li, C. Zhou and D. Lin, *Small*, 2016, **12**, 1702.
33 S. Chen, T. Huang, H. Zuo, S. Qian, Y. Guo, L. Sun, D. Lei, Q. Wu, B. Zhu, C. He, X. Mo, E. Jeffries, H. Yu and Z. You, *Adv. Funct. Mater.*, 2018, **28**, 1805108.
34 C. Qian, L. Li, M. Gao, H. Yang, Z. Cai, B. Chen, Z. Xiang, Z. Zhang and Y. Song, *Nano Energy*, 2019, **63**, 103885–1038892.
35 B. Yao, S. Chandrasekaran, J. Zhang, W. Xiao, F. Qian, C. Zhu, E. B. Duoss, C. M. Spadaccini, M. A. Worsley and Y. Li, *Joule*, 2019, **3**, 459–470.
36 T. Gao, Z. Zhou, J. Yu, J. Zhao, G. Wang, D. Cao, B. Ding and Y. Li, *Adv. Energy Mater.*, 2019, **9**, 1802578.
37 M. Peng, Z. Wen, L. Xie, J. Cheng, Z. Jia, D. Shi, H. Zeng, B. Zhao, Z. Liang, T. Li and L. Jiang, *Adv. Mater.*, 2019, **31**, 1902930.

38 X. Tang, H. Zhou, Z. Cai, D. Cheng, P. He, P. Xie, D. Zhang and T. Fan, *ACS Nano*, 2018, **12**, 3502–3511.
39 Y. Liu, B. Zhang, Q. Xu, Y. Hou, S. Seyedin, S. Qin, G. G. Wallace, S. Beirne, J. M. Razal and J. Chen, *Adv. Funct. Mater.*, 2018, **28**, 1706592.
40 W. Yao, R. Mao, W. Gao, W. Chen, Z. Xu and C. Gao, *Carbon*, 2020, **158**, 418–425.
41 M. Yang, N. F. Zhao, Y. Cui, W. W. Gao, Q. Zhao, C. Gao, H. Bai and T. Xie, *ACS Nano*, 2017, **11**, 6817–6824.
42 Y. N. Ma, Y. Yue, H. Zhang, F. Cheng, W. Q. Zhao, J. Y. Rao, S. J. Luo, J. Wang, X. L. Jiang, Z. T. Liu, N. S. Liu and Y. H. Gao, *ACS Nano*, 2018, **12**, 3209–3216.
43 G. Wu, P. F. Tan, X. J. Wu, L. Peng, H. Y. Cheng, C. F. Wang, W. Chen, Z. Y. Yu and S. Chen, *Adv. Funct. Mater.*, 2017, **27**, 1702493.
44 J. Ren, W. Bai, G. Guan, Y. Zhang and H. Peng, *Adv. Mater.*, 2013, **25**, 5965.
45 J. Meng, W. Nie, K. Zhang, F. Xu, X. Ding, S. Wang and Y. Qiu, *ACS Appl. Mater. Interfaces*, 2018, **10**, 13652–13659.
46 K. Keum, G. Lee, H. Lee, J. Yun, H. Park, S. Y. Hong, C. Song, J. W. Kim and J. S. Ha, *ACS Appl. Mater. Interfaces*, 2018, **10**, 26248–26257.
47 P. Xu, T. Gu, Z. Cao, B. Wei, J. Yu, F. Li, J. Byun, W. Lu, Q. Li and T. Chou, *Adv. Energy Mater.*, 2014, **4**, 1300759.
48 L. Zhang, D. DeArmond, N. T. Alvarez, R. Malik, N. Oslin, C. McConnell, P. K. Adusei, Y. Hsieh and V. Shanov, *Small*, 2017, **13**, 1603114.
49 Y. Meng, Y. Zhao, C. Hu, H. Cheng, Y. Hu, Z. Zhang, G. Shi and L. Qu, *Adv. Mater.*, 2013, **25**, 2326.
50 B. Yao, L. Yuan, X. Xiao, J. Zhang, Y. Qi, J. Zhou, J. Zhou, B. Hu and W. Chen, *Nano Energy*, 2013, **2**, 1071–1078.
51 X. Xiao, X. Peng, H. Jin, T. Li, C. Zhang, B. Gao, B. Hu, K. Huo and J. Zhou, *Adv. Mater.*, 2013, **25**, 5091.
52 G. Wang, H. Wang, X. Lu, Y. Ling, M. Yu, T. Zhai, Y. Tong and Y. Li, *Adv. Mater.*, 2014, **26**, 2676.
53 B. Yao, S. Chandrasekaran, H. Zhang, A. Ma, J. Kang, L. Zhang, X. Lu, F. Qian, C. Zhu, E. B. Duoss, C. M. Spadaccini, M. A. Worsley and Y. Li, *Adv. Mater.*, 2020, **32**, 1906652.
54 W. Wang, W. Liu, Y. Zeng, Y. Han, M. Yu, X. Lu and Y. Tong, *Adv. Mater.*, 2015, **27**, 3572.
55 C. Zhu, T. Liu, F. Qian, T. Y. Han, E. B. Duoss, J. D. Kuntz, C. M. Spadaccini, M. A. Worsley and Y. Li, *Nano Lett.*, 2016, **16**, 3448–3456.
56 Y. Song, T. Y. Liu, G. L. Xu, D. Y. Feng, B. Yao, T. Y. Kou, X. X. Liu and Y. Li, *J. Mater. Chem. A*, 2016, **4**, 7683–7688.
57 H. H. Xu, X. L. Hu, H. L. Yang, Y. M. Sun, C. C. Hu and Y. H. Huang, *Adv. Energy Mater.*, 2015, **5**, 1401882.
58 J. L. Liu, L. L. Zhang, H. B. Wu, J. Y. Lin, Z. X. Shen and X. Wen, *Energy Environ. Sci.*, 2014, **7**, 3709–3719.
59 Y. X. Xu, Z. Y. Lin, X. Q. Huang, Y. Liu, Y. Huang and X. F. Duan, *ACS Nano*, 2013, **7**, 4042–4049.
60 Y. Yue, N. Liu, Y. Ma, S. Wang, W. Liu, C. Luo, H. Zhang, F. Cheng, J. Rao, X. Hu, J. Su and Y. Gao, *ACS Nano*, 2018, **12**, 4224–4232.
61 R. Z. Li, R. Peng, K. D. Kihm, S. Bai, D. Bridges, U. Tumuluri, Z. Wu, T. Zhang, G. Compagnini, Z. Feng and A. Hu, *Energy Environ. Sci.*, 2016, **9**, 1458–1467.
62 L. Li, J. Zhang, Z. Peng, Y. Li, C. Gao, Y. Ji, R. Ye, N. D. Kim, Q. Zhong, Y. Yang, H. Fei, G. Ruan and J. M. Tour, *Adv. Mater.*, 2016, **28**, 838.
63 Y. Liu, B. Weng, Q. Xu, Y. Hou, C. Zhao, S. Beirne, K. Shu, R. Jalili, G. G. Wallace, J. M. Razal and J. Chen, *Adv. Mater. Technol.*, 2016, **1**, 1600166.
64 Z. Wu, K. Parvez, S. Li, S. Yang, Z. Liu, S. Liu, X. Feng and K. Müllen, *Adv. Mater.*, 2015, **27**, 4054.
65 Y. Zhang, W. Fan, Y. Huang, C. Zhang and T. X. Liu, *RSC Adv.*, 2014, **5**, 1293–1301.

